Article

Weaker absorption of Asian dust than previously estimated based on observation-constrained simulation

Check for updates

Youjia Yuan[1,2], Hao Wang[3], Chenglai Wu[3,4], Tafeng Hu[5], Feng Wu[5], Daizhou Zhang[6] & Junji Cao[1,7] ✉

Dust aerosols constitute a major component of shortwave-absorbing aerosols, with absorption uncertainties predominantly associated with mineral composition variations. To address this, we analyzed 22 East Asian dust (EAD) samples and derived a revised imaginary part of the complex refractive index (k), with a range spanning from 2.26×10^{-4}–8.37×10^{-4} in 0.3–1 μm, which is significantly lower than the Optical Properties of Aerosols and Clouds (OPAC) and the values commonly used in research on East Asian. The improved optical parameters applied to CAS-ESM2 for spring dust simulations have been shown to reduce single scattering albedo (SSA) bias from 15% to 2% and absorption aerosol optical depth (AAOD) overestimation from +5.2% to −1.7%. The modified scheme reduces atmospheric absorption by 79.5% (−7.61 W/m²) and reverses the top of atmospheric shortwave radiation effect to −3.80 W/m². This outcome revealed that dust absorption in East Asia is weak and the climate impact is significantly different from previous assessments.

Mineral dust, principally originating from global arid and semi-arid regions, constitutes the dominant atmospheric aerosol by mass on Earth[1]. The influence of this aerosol on climate is complex and yet to be fully quantified. At present, the magnitude of the radiative effect of dust aerosols remains highly uncertain[2], and the specific local radiation effects are regulated by multiple factors, including particle size distribution, the iron oxide content, and surface albedo[3,4]. Therefore, enhancing our understanding of the shortwave absorption characteristics of dust can provide new insights into revealing the magnitude of radiation effect caused by mineral dust[5]. However, due to insufficient understanding of the key parameter k describing the absorption characteristics of dust aerosols and the important parameter SSA characterizing the ratio of absorption to scattering capacity, the representation of relevant microphysical properties in climate models remains highly uncertain[6,7].

k for dust can be determined through various methods. Numerous studies on Saharan dust have derived representative k through laboratory measurements with theoretical calculations on field-collected samples[8–10]. In contrast, the study of Asian dust is relatively limited. The existing Asian dust k estimates are derived through dust

component analysis with corrections[11,12] and combined satellite observations and models[13]. While their k are of a similar magnitude, East Asian dust particles are finer and exhibit stronger backscattering capabilities[14]. Furthermore, their iron oxide content is lower than that of North African dust[15]. Whether these commonly used optical parameterization schemes are applicable in the East Asian region requires further investigation. In addition, past observations of EAD primarily relied on single or sparse soil samples and atmospheric data collected during dust events[15]. This approach failed to accurately characterize key absorbing minerals in East Asia, leading to substantial bias in radiation effect estimates.

This study utilizes a total of 22 surface soil samples obtained from East Asian dust source regions, in conjunction with meticulous model validation, to formulate a region-specific dust complex refractive index scheme for East Asia. The implementation of this scheme within a Global Climate Model (GCM) yields simulations that demonstrate enhanced congruence with ground-based station observations. The results further reveal significant discrepancies in the estimated shortwave direct radiative effect of East Asian dust aerosols compared to previous assessments.

[1]State Key Laboratory of Atmospheric Environment and Extreme Meteorology (AEEM), Institute of Atmospheric Physics, Chinese Academy of Sciences, Beijing, China. [2]University of Chinese Academy of Sciences, Beijing, China. [3]International Center for Climate and Environment Sciences, Institute of Atmospheric Physics, Chinese Academy of Sciences, Beijing, China. [4]State Key Laboratory of Earth System Numerical Modeling and Application, Institute of Atmospheric Physics, Chinese Academy of Sciences, Beijing, China. [5]State Key Laboratory of Loess Science, Institute of Earth Environment, Chinese Academy of Sciences, Xi'an, 710061, China. [6]Faculty of Environmental and Symbiotic Sciences, Prefectural University of Kumamoto, Kumamoto, 862-8502, Japan. [7]Science Center for Earth System Numerical Simulation, Institute of Atmospheric Physics, Chinese Academy of Sciences, Beijing, China. ✉e-mail: jjcao@mail.iap.ac.cn

Results

k of EAD constrained by laboratory measurements

Iron oxides in mineral dust are predominantly present as hematite or goethite, with their relative abundances depending on the pedogenic conditions of the source regions[16]. Other types of light-absorbing oxides co-exist in dust aerosols, but their overall content is usually negligible when considered against the significance of hematite and goethite in the short-wave spectral range for dust absorption. These minerals exhibit strong absorption capacity in the UV-visible spectral region[15], making them key contributors to the radiative properties of dust aerosols despite their relatively low mass fractions. This is of particular significance when the minerals are internally mixed with other minerals that exhibit lower levels of absorption[17]. Therefore, accurately reflecting the optical properties of these minerals is essential to reduce the uncertainty of dust-climate feedback[5]. Analysis of soil samples from 22 sites across major EAD source regions—Gobi Desert, Taklimakan Desert, and Qaidam Basin (Fig. 1c), which reveals regional variability in the mass percentage of iron oxide ($MC^s_{Fe-ox\%}$) (Fig. 1a). $MC^s_{Fe-ox\%}$ were found to be comparatively low throughout East Asia; however, higher values were observed in the western desert regions of China. These findings suggest a potential correlation with the surface material composition, degree of weathering, and climate-driven soil-forming processes at the sampling sites. The Gobi Desert exhibits the lowest mean

content (0.74 ± 0.004%), the Taklimakan Desert intermediate (0.77 ± 0.002%), and the Qaidam Basin the highest (0.89 ± 0.005%).

Based on soil samples and the established correlation between $MC^s_{Fe-ox\%}$ and k in the short-wavelength band[10], the wavelength-dependent variation of k was derived (Fig. 1b). It has been discovered that the absorption characteristics of EAD are weak in the short-wave spectrum (0.3–1 μm), and k range from 2.26×10^{-4} to 8.37×10^{-4}, which is significantly lower than the value in the OPAC database constructed by Sahara dust measurement[18]. Furthermore, it is pointed out by previous studies that the numerical differences of k used in the model vary from five times to one order of magnitude in the spectral range of 0.3 to 30 μm[19]. It is evident that this reflects the high level of uncertainty in the current characterization of the optical properties of mineral dust. The k of East Asia obtained by combined observation is 0.00042 at 550 nm wavelength, which is over one order of magnitude below the OPAC value used by NASA/GEOS[20] (Fig. 2b: Colarco et al.[20]) and the intermediate k value of 0.003 used by WRF-Chem model in standard experimental simulation[21–23]. This result further confirms the significant differences in the optical properties of dust between regions, and suggests that the traditional global model may systematically overestimate the radiation effect of EAD due to over-reliance on single, overestimated absorption parameters. However, it is only marginally higher than observations of long-range transported dust in Seoul[15],
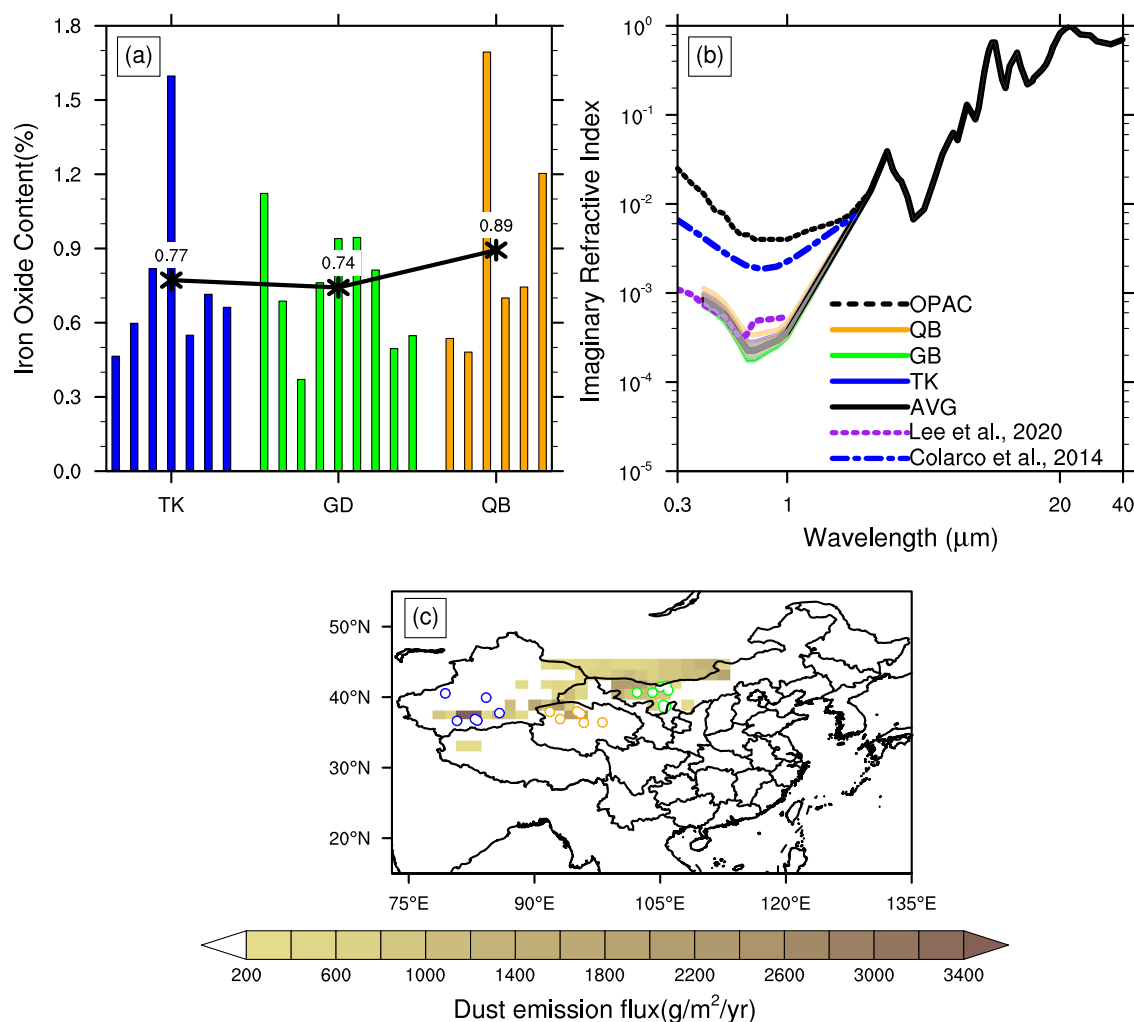

Fig. 1 | Total particulate iron oxide mass percentages, imaginary part of the complex refractive indices across East Asian dust source regions, and distribution of soil sampling sites. a The total particulate $MC^s_{Fe-ox\%}$ were calculated at 22 sampling sites. **b** Wavelength-dependent distribution of k. Comparative data include: mineral dust complex refractive indices from the OPAC database (black dashed line), the observationally derived refractive index by Colarco and Kim (blue dashed line) and the observationally calculated refractive index by Lee (purple dashed line). **c** Spatial distribution of sampling sites and dust emission fluxes. All sites are proximal to dust source regions.
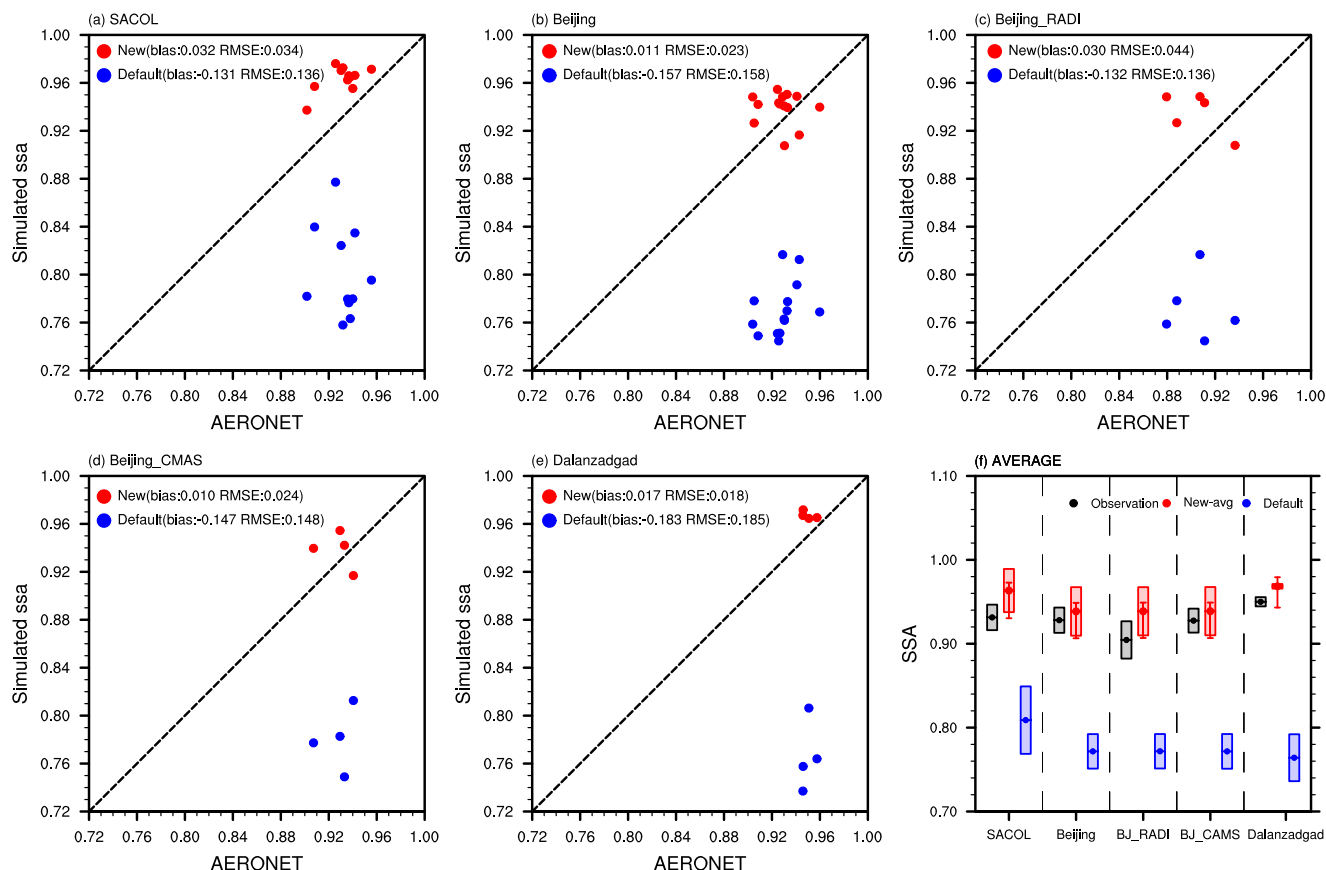
Fig. 2 | Observation-constrained simulations effectively ameliorate the under-estimation of SSA in the default model scheme. a–e Comparison between 550 nm SSA simulations from two experiment (Default: blue dots; New-avg: red dots) and AERONET-derived 550 nm SSA at five sites. **f** Comparison of observed SSA means (dots) with four experimental groups. Shaded areas denote ±1 standard deviation. Mean values for New-p90 and New-p10 are indicated by upper/lower red horizontal dashes.

Effective improvement of optical parameters

In order to rigorously assess the degree of improvement of the new parameterization of the optical properties of dust, the five stations located at or near the dust source regions were selected for comparison according to the standard that the station was mainly affected by dust. The SSA simulation results of the Default experiment and the New-avg experiment are compared with the results of AERONET at the wavelength of 550 nm, and it is found that the latter is very consistent with the results of AERONET. This phenomenon is evidenced by two salient statistical indicators: firstly, the mean relative bias of the five sites has been diminished from 15% to 2%, and secondly, the root mean square error (RMSE) has been substantially reduced by an order of magnitude (Fig. 2a–e), with the most substantial enhancement occurring at the Beijing site, which is not only data-rich, but also exhibits a high degree of similarity to the observed data. Furthermore, the simulation outcomes of the new scheme at the SACOL and Dalanzadgad stations, which are situated within the dust source region, have been significantly enhanced, though they do exhibit a slight discrepancy when compared to the observational results. Additionally, simulations from the New-p90 and New-p10 experiment results exhibit more pronounced improvements at specific sites (Figs. S1, S2).

The statistical results indicate that the Default experiment significantly underestimated the SSA, with mean underestimations of 0.12 (SACOL), 0.16 (Beijing), 0.13 (Beijing_RADI), 0.16 (Beijing_CMAS), and 0.19 (Dalanzadgad) (Fig. 2f). In contrast, the three new schemes' mean SSA values (red dots and short dashes) align better with observations in overall

trend and variability range. The presence of at least one mean point at each site (across the three sets of experiments of the new scheme) falling within one standard deviation of the observed values (the black shaded area) indicates that the systematic bias of the new parameterization scheme has been largely contained within the dominant range of random errors.

It is vital to note the dependence of AAOD on dust extinction, which can be measured using AOD. Furthermore, the absorption proportion in this extinction can be determined by SSA[24]. The Default experiment (dashed lines) systematically overestimates the AAOD of 550 nm at three key sites (i.e., SACOL, Beijing, and Dalanzadgad) (Fig. 3a–c). In contrast, the observationally constrained New-avg experiment (solid lines) aligns closely with site observations (dots). This improvement stems from more accurate characterization of iron oxides, which are the key absorption components in mineral dust, and reduces the root mean square error (RMSE) by 43.2%, 55.2% and 93.2% at the three locations of AAOD, respectively.

However, by comparing AOD values, as shown in Fig. S3, we also conclude that this bias likely stems from issues such as dust emission, transport and deposition, as current free-running atmospheric model that is not nudged would result in biases in wind fields and precipitation fields. Additionally, the missing larger particles ($>10\mu m$) in the model may lead to an underestimated AOD in the visible spectrum. Moreover, when focusing on total dust optical depth (DOD), although both simulations exhibit a systematic positive bias relative to satellite retrievals, particularly pronounced over East Asian dust source regions, their spatial distribution patterns remain broadly consistent. The new parameterization scheme yields regional mean values closer to satellite observations (Fig. S4).

Finally, spatial distributions (Fig. 3d–e) further indicate significant overestimations by the Default experiment across EAD sources (e.g., TD,
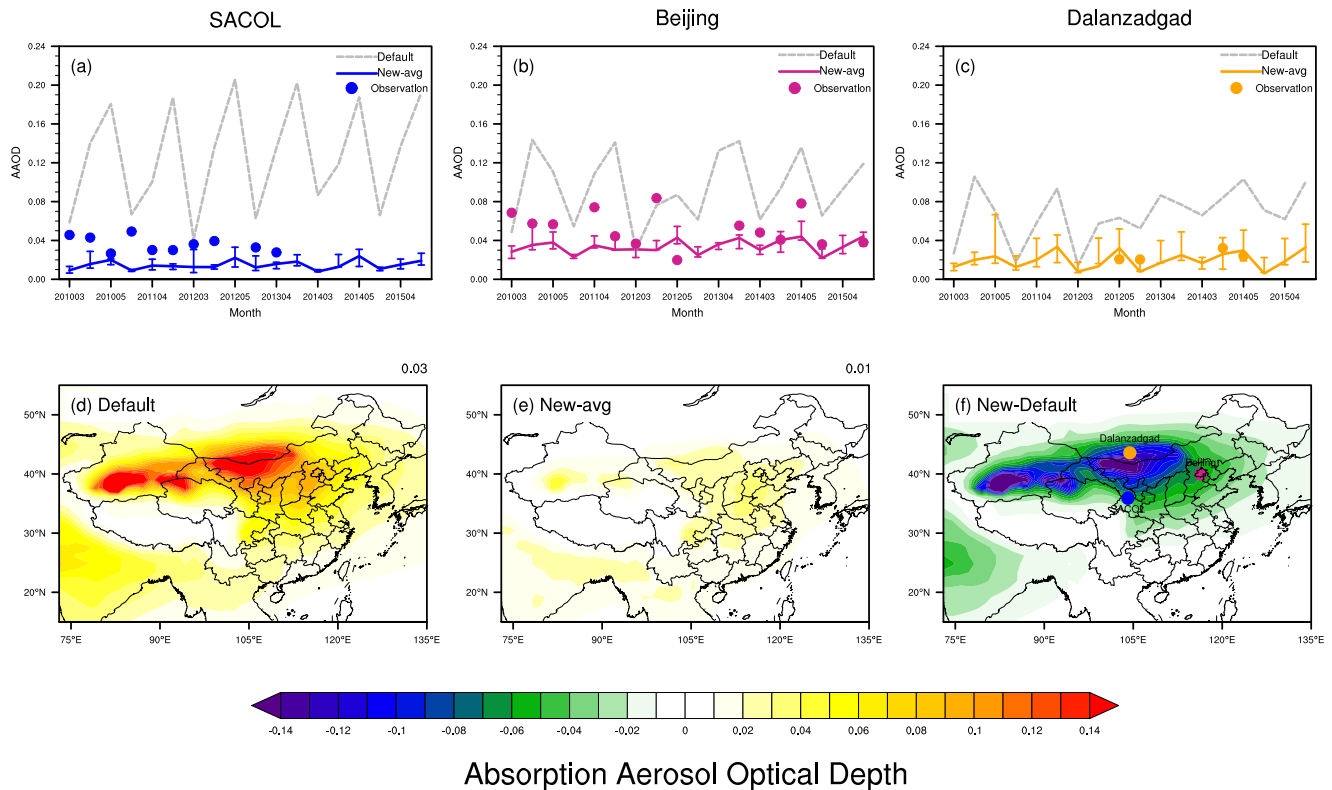
Fig. 3 | Observation-constrained simulations effectively mitigate overestimation of absorbing optical depth in the default model scheme. a–c Temporal evolution of AAOD simulated in two experiments: New-avg (solid lines) and Default (dashed lines), compared with AERONET observations at SACOL (blue dots), Beijing (magenta dots), and Dalanzadgad (yellow dots). upper/lower horizontal dashes in corresponding colors denote mean values from New-p90 and New-p10 experiments. **d–f** Spatial distribution of AAOD and its difference between the two experiments.

Mongolian Plateau) as well as their downstream regions (e.g., North China Plain). Moreover, the difference between the two groups of experiments in the western desert and the northern desert can reach more than -0.14, that is, there is a more obvious improvement in the dust source area. The Dalanzadgad station, situated in proximity to the area exhibiting substantial variations, has yielded a limited number of observations. However, these observations demonstrate a high degree of similarity with the new parameter scheme. The New-avg experiment constrains the regional mean AAOD to 0.0106 (0.0093-0.0132) by 65.4% compared with the default scheme.

Assessment of short-wave DRE in East Asia

The New-avg experiment reveals markedly distinct radiative effects compared to the Default experiment. This shift is particularly evident in the enhanced cooling effect at the top of the atmosphere (TOA): the revised scheme adjusts SW direct radiative effect (DRE) from $+0.75$ W/m^2 (Fig. 4a) to -3.80 W/m^2 (Fig. 4d). Despite numerical differences, it aligns with prior estimates of shortwave radiative cooling by EAD aerosols[12,22,23]. Crucially, we constrain the k to 10^{-4} through extensive observations, providing a more reliable data foundation compared to the commonly adopted 10^{-3} to 10^{-2} range (Table 1). Further analysis of changes in surface (SFC) direct radiation effect shows that the revised scheme diminishes surface radiative cooling by 34.6% (Fig. 4i), but this reduction is notably less pronounced than the TOA radiative effect sign reversal and the 79.5% attenuation in atmospheric absorption (Fig. 4h). Overall, it shows that the absorption capacity of EAD is weak, which may be related to the significant difference in optical characteristics between EAD and Sahara dust. The former has a strong back-scattering ability, which leads to a higher negative value of shortwave radiation effect at the TOA[11].

Spatially, the dust radiative effect exhibits pronounced regional characteristics. Regions of intense shortwave radiative cooling at the TOA (≥ -18

W/m^2) are predominantly localized near dust source regions, exemplified by the Taklimakan and Badain Jaran Deserts. In these regions, the simulated maximum SW DRE at the SFC under the new parameterization scheme reaches -27 W/m^2, slightly exceeding the -25 W/m^2 reported in similar studies[25,26]. Moreover, there is also a certain improvement in the downwind region of its transmission, extending to other seas such as the Yellow Sea and the East China Sea, where radiative cooling of the TOA has occurred. Additionally, the simulated TOA shortwave radiative cooling over the Tibetan Plateau is stronger, with a regional average of -5.63 (-6.37 to -4.48) W/m^2, also higher than other estimates[22,23], which confirms that robust scattering processes over EAD sources exert significant influences on local climate. On the time scale, the dust cooling effect is stronger in 2010 and 2014, and the regional average of SW radiation effect at the TOA is -4.45 W/m^2, which is about 22% higher than the regional average of -3.47 W/m^2 in other years (Table S4). This systematic quantification provides critical scientific insights into the DRE of EAD.

Discussion

Currently, GCMs exhibit high uncertainty in both projections of future dust emissions and climate-dust feedbacks[5]. This leads to aerosol radiative effect as an uncertainty in current Earth energy balance studies. To address the problem of overestimation of dust aerosol absorptive properties in climate models for East Asia, this study developed region-specific k using 22 soil samples covering most of the dust source regions, combined with rigorous model validation methods. Moreover, the shortwave DRE in East Asia was reassessed, and it was found that the absorptive properties of EAD are weaker than the previous estimates. The cooling effect of SW radiation is more pronounced near the dust source area and in the downwind region.

However, in simulating particle size distribution and dust emission processes, this study employs multiple log-normal distributions for simplified estimation of $p_m(d)$ and $p_f(d)$ (Eq. 3) due to the lack of a complete soil
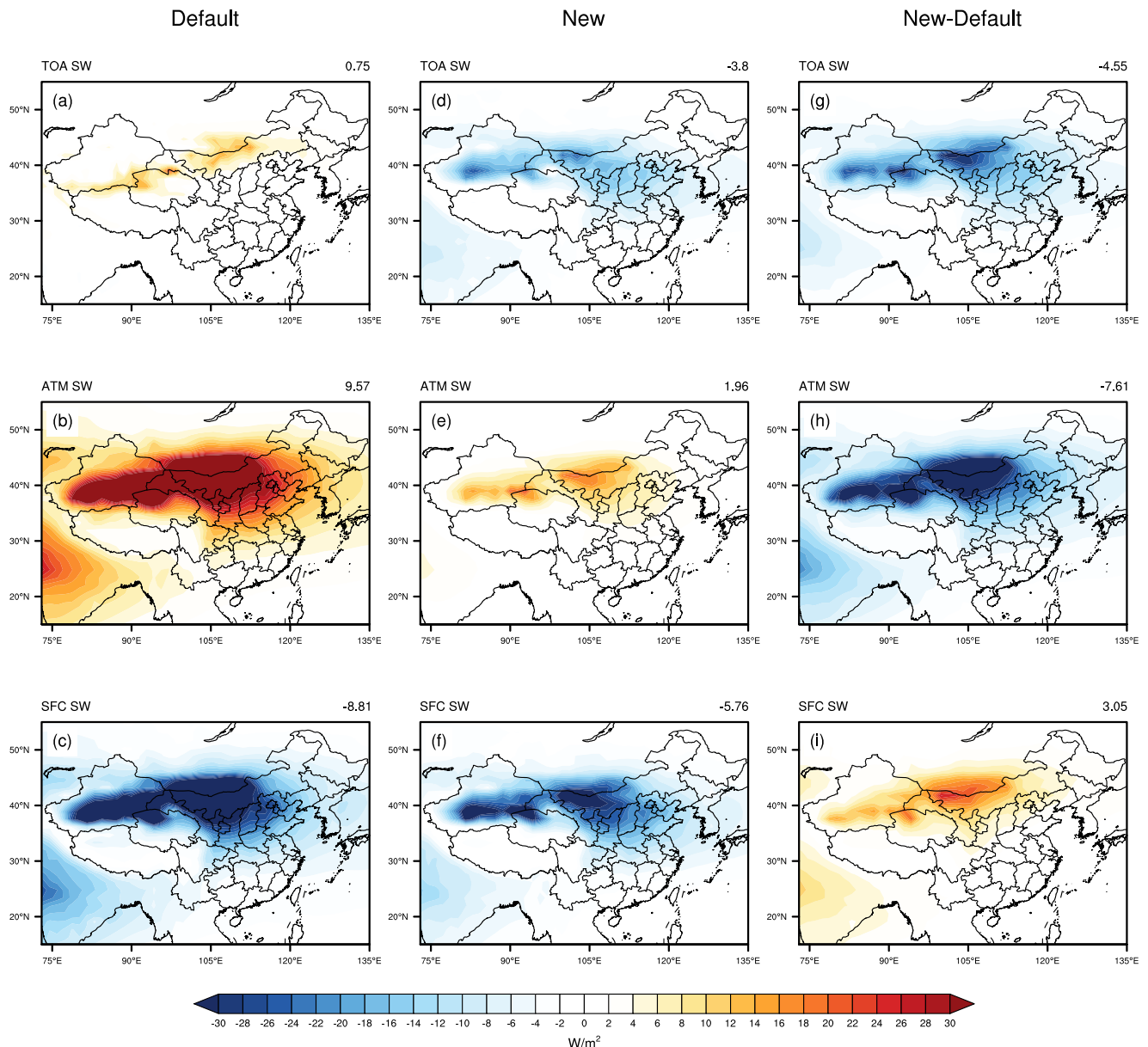
Fig. 4 | The spatial distributions of dust shortwave (SW) direct radiative effect. **a**–**c** the Default experiment of OPAC scheme, (**d**–**f**) New-avg experiment of updated scheme and their dust shortwave radiation effect at the TOA, ATM and SFC respectively. **g**–**i** Difference between the two sets of experiments. Significant differences have occurred at the TOA, where radiative effect exhibits sign reversal. Concurrently, atmospheric absorption is substantially attenuated.

sample dataset in the Shao04 scheme. The actual distribution varies with soil type, wind speed, and transport processes, and spatial variability is not accounted for. In addition, significant uncertainties are not only present in the characterization of surface soil conditions in dust source regions, but are also widespread in several key aspects of the transport phase. For example, the characterization of processes dust–cloud interactions, the treatment of dry and wet deposition, and the mixing state with other aerosols is still not precise enough, limiting the accuracy of model simulations of dust and its climatic effects.

Particle size distribution is considered to be an important parameter that strongly affects the DRE of dust[27], but the problem of its characterization remains unresolved to date[28]. Therefore, although the complex refractive index of minerals itself does not change with particle size[17], that is, the optical properties of minerals remain constant at different particle sizes, the SSA gradually decreases as the proportion of coarse-grained dust increases. However, there are still major challenges in the characterization of dust size distributions in current models, and related problems have not

been effectively solve[27]. Since coarse particles of dust have a stronger absorption capacity and shorter lifetime than fine particles, we set the cut-off diameter of aerosols to 10 μm in the CAS-ESM2 model, and the geometric diameter range (0.1–10 μm) considered in the model fails to cover the true distribution[29], i.e., the contribution of coarse particles may be excluded, leading to an underestimation of the warming effect of dust[2]. Previous studies have attempted to incorporate spatiotemporal variations in mineral composition[30], the impact of super-coarse particles[31], or the effects of different mixing rules on dust optical properties[7] into models. These represent areas warranting further investigation in subsequent research.

Additionally, dust exhibits a non-negligible warming effect in the longwave band[32]. Uncertainties in the DRE of long waves arise mainly from the complex refractive index of mineral particles, their size distribution and their vertical distribution in the atmosphere, rather than from the mineral composition itself[28]. This means that even if the relative content of various minerals changes, the effect on long-wave radiation is relatively weak and shows a low sensitivity. Furthermore, since iron oxides are less significant in

Table 1 | Comparison of shortwave direct radiation effect and complex refractive index scheme of EAD with previous studies

TOA(W/m²)	ATM (W/m²)	SFC (W/m²)	Time	Region	Refractive Index	The magnitude of $k(0\text{-}1\mu m)$	Reference
−3 (SW)	–	−17(SW)	5–15 Apr. 2011	Asian Pacific Regional	Corrected OPAC^a (CFORS &Monte Carlo^b)	10^{-3}–10^{-2}	Conant et al.[12]
−1.7(SW)	–	−6.25(SW)	Spring 2001	EANP^c region	ADEC^d (LASG GCM)	10^{-3}–10^{-2}	Wang et al.[11]
Up to −7.5 (SW)	–	Up to −25 (SW)	FMAM^e 1997–2006	East Asian deserts	OPAC (RegCM3^f)	10^{-3}–10^{-2}	Zhang et al.[26]
Up to −8 (SW)	–	Up to −25 (SW)	Spring 2000–2009	TD and GD	OPAC (RegCM4)	10^{-3}–10^{-2}	Sun et al.[25]
−5.02 (SW)	6.69 (SW)	−11.71 (SW)	26–30 July 2006	TD and TP	1.53 + 0.003i^g (WRF–Chem)	10^{-3}	Chen et al.[22]
−4	3	−7	2007–2011	East Asia	1.53 + 0.003i (WRF–Chem)	10^{-3}	Chen et al.[54]
−1.4(SW)	0.67(SW)	−2.08(SW)	2010–2015	Tibet Plateau	1.53 + 0.003i (WRF–Chem)	10^{-3}	Hu et al.[23]
−3.79(SW) (**−3.01 to −4.19**)	1.96(SW) (**1.41 to 2.90**)	−5.76(SW)(**−5.90 to −5.60**)	Spring 2010–2016	East Asia	0.00042i at 550 nm (CAS-ESM2)	10^{-4}–10^{-3}	This study

The bold values indicate the range of shortwave direct radiative effects (TOA, ATM, and SFC) derived from this study.

^a Combined with the observed data, a coated (two-layer) sphere solution to light scattering and ISORROPIA aerosol chemical equi-librium model are adopted to correct the different values of OPAC data and observed data.

^b Monte Carlo Radiative Transfer Model.

^c East Asia-north Pacific.

^d The Sino-Japanese collaborative project "Studies on the Origin and Transport of Aeolian Dust and Its Effects on Climate" (ADEC) acquired the complex refractive index of East Asian dust. This was achieved through a weighted average complex refractive index of minerals, combined with diffuse fraction measured in the field and theoretical calculation results, finally a modified complex refractive index was obtained.

^e February–March–April–May (FMAM).

^f Regional Climate Model RegCM version 3.

^g According to previous studies, the imaginary part (k) of complex refractive index is in the range of 0.0004 to 0.006 near the wavelength of 550 nm[21], but the estimated values are still quite different. The intermediate value simulated by multiple experimental standards is 0.003.

the longwave band compared to minerals like quartz and clay[28], and their imaginary part of the refractive index exhibits smaller variations in the longwave band relative to the visible spectrum[33], this study focuses on shortwave radiation effects. Based on data availability and phased objectives, it lays the groundwork for integrating longwave effects in subsequent research.

The influence of dust aerosols on the atmospheric circulation[34,35] and weather systems mainly stems from their perturbation of the energy balance at the surface and in the uplift layer[34,36], which may not only alter the atmospheric stability[37], but also affect the horizontal temperature gradient. Particularly in the springtime, when dust storms are frequent, the extension from the Taklamakan Desert to North China and other downwind areas may experience significant changes in the DRE of dust, making these regions key areas for studying dust-climate interactions. Since changes in meteor-ological conditions can in turn affect the dust release and transport processes[37], this study improves the accuracy of the estimation of the optical properties of dust by introducing the constraint of iron oxides on the k of dust, which is more helpful for realistically simulate the radiative effect of mineral dust and its feedback role in the dust cycle.

Methods

Soil sample collection

Dunes and gravel soils represent different surface conditions of desert terrain and may be the main sources of desert atmospheric dust[38]. This study collected 22 soil samples from typical sand dune and gravel desert surfaces in China's major dust source areas. Detailed information on the locations and surrounding geomorphology of the sampling sites is listed in Table S1.

Laboratory assay

The dust mobilization system generates mineral dust aerosol particles from the collected sample soil by simulating natural processes such as dust sandblasting and saltation[39]. The chemical composition and particle size distribution are the same as those in the field[40].

Computer-controlled scanning electron microscopy (CCSEM) allows for the analysis of atmospheric particulate matter by characterizing the properties of air masses through the detection of the morphology and composition of thousands of individual particles[41]. The CCSEM system employs the rotating Ferret box method to measure particle diameter (Fig. S5), thereby calculating detailed morphological parameters such as aspect ratio and particle roundness[42]. It also determines the weight percentage of elements based on their characteristic X-ray signals[43]. The system can classify particles according to both morphological parameters and elemental composition, with its data complementing results from bulk analysis techniques. Traditionally, particle classification within this system relies on hierarchical rules that group particles with similar characteristics by integrating elemental concentrations and morphological parameters. The particle classification rules are listed in Table S2 [44]. The empirical formula and elemental composition information are available in the handbook of mineralogy[45] and several online databases at https://duffy.princeton.edu/mineralogy-and-crystallography-databases. This study focuses on the percentage of iron oxide mass of each sample, so single-particle iron oxides need to be treated. The specific formula is expressed as follows:

$$MC^s_{Fe-ox\%} = \frac{\sum_{i=1}^{n} M_{Fe-ox}}{\sum_{j=1}^{m} M_{sp}} \quad s = 0, 1, 2 \ldots \ldots 22 \quad (1)$$

where n is the number of single-particle iron oxides, M_{Fe-ox} is a mass of single-particle iron oxide, m is the total count of particles in each sample, M_{sp} is a total mass of all particles.

Complex refractive index of dust

Evidence indicates a pivotal role for the composition of iron oxides in determining the optical properties of dust[46]. Within the 0.3–1 μm wavelength range, $MC^s_{Fe-ox\%}$ exhibits a strong correlation with k[10]. In this study, the robust correlation between them is adopted. The formula used to

calculate k is as follows:

$$k_{s,\lambda} = a_\lambda \times MC_{Fe-ox\%}^s + b_\lambda \quad \lambda = 370, \ldots 950\,nm \quad (2)$$

Here, the coefficients a and b are defined as linear fitting parameters[10] and consist of data from six different bands; s denotes the sample serial number.

CAS-ESM2

CAS-ESM2 employs a modular architecture, including several independent component models such as land and atmosphere. These components are coupled via the CPL7 coupler to exchange physical quantities and enable synchronized simulation[47]. The simulations follow the protocols of the Atmospheric Model Intercomparison Project, incorporating prescribed sea surface temperature, precursor emissions, and anthropogenic aerosol data. It has a horizontal resolution of $1.4° \times 1.4°$ and a vertical coordinate of 35 layers of atmospheric hybrid sigma-pressure. Four sets of simulation results were used, including one control experiment (Default) utilizing the default OPAC data and three additional experiments utilizing observation-constrained new schemes based on the mean (New-avg), 90th percentile (New-p90), and 10th percentile (New-p10) values. The model runs from January 2006 to December 2015, with the initial four years designated as the spin-up period and the subsequent six years used for analysis. During the summer and autumn seasons, dust particles are influenced by East Asian monsoon precipitation and are also susceptible to mixing with anthropogenic aerosols. This weakens the dust radiation effect signal and increases uncertainty in the model decoupling. To ensure analytical accuracy and avoid making highly uncertain inferences, the simulation results for the primary dust-generating months (March to May) between 2010 and 2015 were compared with the more abundant, quality-controlled spring observations from AERONET.

The Shao04 dust emission scheme has been introduced into the Common Land Model (CoLM), thereby enabling the CAS-ESM2 model to produce a more complete representation of land-atmosphere interactions[48]. This parameterization scheme calculates dust emissions generated by saltation impacts across varying particle sizes. Based on the USDA soil texture classification, the soil particle size distributions ($p_m(d)$ and $p_f(d)$) are represented as multi-lognormal combinations. This approach makes the emitted dust particle size distribution dependent on both surface soil properties and dynamic processes, yielding good agreement with field observations[49]. The present study configures the fifth-generation atmospheric general circulation model developed by IAP (IAP AGCM5) with CoLM, implementing the Shao04 dust emission scheme for dust process simulations. The calculation of dust emission fluxes is performed in CoLM, and these data are subsequently transferred to IAP AGCM5, where the Bulk Aerosol Module (BAM) is utilized. Aerosol size distributions are grouped into four size bins. Each bin is assumed to follow a log-normal distribution, thereby ensuring the preservation of particle size information[50,51]. From a climate-scale perspective, the atmospheric residence time of coarse particles is typically shorter, which often attenuates the cumulative effects of long-term climate feedback. Consequently, in our simulations, we primarily employed a universal particle size distribution (0-10 μm). The following formula is employed to calculate dust particle emission flux:

$$F(d_j, d_i) = c_y \eta_{fj} \left((1-\gamma) + \gamma \frac{p_m(d_j)}{p_f(d_j)} \right) \frac{Q(i)g}{u_*^2} (1 + \sigma_m) \quad (3)$$

$$\sigma_m = 12u_*^2 \frac{\rho_p}{p} \left(1 + 14u_* \sqrt{\frac{\rho_p}{p}} \right) \quad (4)$$

In this equation, c_y is a coefficient without dimensions, η_{fj} denotes mass-specific gravity, γ represents a weighting factor linked to the particle size distribution, and $p_m(d_j)$ and $p_f(d_j)$ are the minimum and maximum disturbance to the particle size distribution, correspondingly. The quantity $Q(i)$ is employed to measure the flux of sand particles with a diameter of d_i. The gravitational acceleration constant g is also considered, while the symbol u_* is used to denote the friction speed. The parameter σ_m is defined as the efficiency of the bombardment process.

Subsequently, based on the effective radii of four size bins in the bulk aerosol module and the newly estimated k, the dust optical parameters (including mass extinction coefficient, single-scattering albedo, and asymmetry factor) for the 14 shortwave bands required by the RRTMG radiation scheme were calculated using Mie scattering theory. These parameters replaced the dust optical parameters calculated using OPAC and were simulated using the Chinese Academy of Sciences Earth System Model Version 2 (CAS-ESM2). Each shortwave band covers a specific wavelength interval to capture the critical absorption and scattering behavior of dust in solar radiation. This method is based on the spherical particle assumption and is generally suitable for radiative transport modeling of sand and dust aerosols. Furthermore, it is imperative to undertake a diagnostic calculation to ascertain the instantaneous DRE of dust aerosols. This involves removing the species from all modes that contain it. A new mode definition excluding dust aerosols is created based on the default definitions. The distinction between these two configurations is pivotal in diagnosing dust's SW DRE. The specific formula is as follows:

$$R_T = \Delta FS_{TD} - \Delta FS_{TN} \quad (5)$$

$$R_S = \Delta FS_{SD} - \Delta FS_{SN} \quad (6)$$

In this equation, R denotes the calculated radiative effect; subscripts T and S represent the TOA and the SFC, respectively; D and N denote the default definition containing dust aerosols, as well as the new definition without dust aerosols; and ΔFS represents the shortwave radiative flux at a given level.

AERONET

AERONET is a network specifically designed for the monitoring of aerosols. It was established by NASA (United States) and CNRS (France)[52]. The present study employs Level 2.0 dataset (high-quality assured), encompassing SSA, AAOD, aerosol optical depth (AOD), and Ångström exponent (AE) at a spatial resolution of 15 min.

Specifically, the dataset utilized includes AOD, SSA, and AAOD at the 550 nm wavelength band (denoted as AOD_{550}, $AAOD_{550}$, and SSA_{550}, respectively) and the AE over the 440–870 nm wavelength band (denoted as $AE_{440-870}$). The AOD_{550}, $AAOD_{550}$ and SSA_{550} values are derived through logarithmic interpolation of data from the 440 nm and 675 nm wavelength bands. As illustrated in Table S3, the study incorporates a comprehensive inventory of the AERONET sites used in this investigation, accompanied by their geographical locations and temporal coverage. To ensure data quality, the following screening criteria are applied: instances where the AOD at 440 nm is elevated ($AOD_{440} \geq 0.4$) and the AE over the 440–870 nm band is diminished ($AE_{440-870} < 0.6$) are classified as predominantly influenced by dust aerosols on that particular day[53]. Although this method enhances the significance and fidelity of dust signals, residual non-dust pollution remains difficult to quantify.

Data availability

The laboratory-measured data on iron oxide mass percentages and the CAS-ESM2 simulation output data are obtainable upon reasonable request from the relevant author. Complex refractive indices used here are available from Lee et al.[15], Colarco et al.[20], and Hess et al.[18]. The AERONET data are downloaded from https://aeronet.gsfc.nasa.gov/new_web/download_all_v3_inversions.html, last accessed: 8 May 2025.

Code availability

The NCL scripts used for data processing can be obtained through reasonable application to the author.

References

1. Shao, Y. et al. Dust cycle: an emerging core theme in Earth system science. *Aeolian Res.* **2**, 181–204 (2011).
2. Kok, J. F. et al. Smaller desert dust cooling effect estimated from analysis of dust size and abundance. *Nat. Geosci.* **10**, 274–278 (2017).
3. Kok, J. F. et al. Mineral dust aerosol impacts on global climate and climate change. *Nat. Rev. Earth Environ.* **4**, 71–86 (2023).
4. Castellanos, P. et al. Mineral dust optical properties for remote sensing and global modeling: a review. *Remote Sens. Environ.* **303**, 113982 (2024).
5. IPCC. *PCC, 2021: Climate Change 2021: The Physical Science Basis. Contribution of Working Group I to the Sixth Assessment Report of the Intergovernmental Panel on Climate Change* (Cambridge University Press, 2023). https://doi.org/10.1017/9781009157896.
6. Samset, B. H. et al. Aerosol absorption: progress towards global and regional constraints. *Curr. Clim. Change Rep.* **4**, 65–83 (2018).
7. Li, L. et al. Improved constraints on hematite refractive index for estimating climatic effects of dust aerosols. *Commun. Earth Environ.* **5**, 295 (2024).
8. Müller, T., Schladitz, A., Kandler, K. & Wiedensohler, A. Spectral particle absorption coefficients, single scattering albedos and imaginary parts of refractive indices from ground based in situ measurements at Cape Verde Island during SAMUM-2. *Tellus B: Chem. Phys. Meteorol.* **63**, 573–588 (2011).
9. Kim, D. et al. Dust optical properties over North Africa and Arabian Peninsula derived from the AERONET dataset. *Atmos. Chem. Phys.* **11**, 10733–10741 (2011).
10. Di Biagio, C. et al. Complex refractive indices and single-scattering albedo of global dust aerosols in the shortwave spectrum and relationship to size and iron content. *Atmos. Chem. Phys.* **19**, 15503–15531 (2019).
11. Wang, H., Shi, G., Teruo, A., Wang, B. & Zhao, T. Radiative forcing due to dust aerosol over east Asia-north Pacific region during spring, 2001. *Chin. Sci. Bull.* **49**, 2212–2219 (2004).
12. Conant, W. C. et al. A model for the radiative forcing during ACE-Asia derived from CIRPAS Twin Otter and R/V *Ronald H. Brown* data and comparison with observations. *J. Geophys. Res.* **108** (2003).
13. Hagihara, Y., Fukushima, H., Uno, I. & Ohta, S. Evaluation of Asian dust absorption in visible band with satellite observation, sky-radiometer measurement, and chemical transport model. *Sola* **2**, 120–123 (2006).
14. Jin, Q., Wei, J., Yang, Z.-L., Pu, B. & Huang, J. Consistent response of Indian summer monsoon to Middle East dust in observations and simulations. *Atmos. Chem. Phys.* **15**, 9897–9915 (2015).
15. Lee, K., Choi, H. & Kim, J. Refractive index for asian dust in the ultraviolet-visible region determined from compositional analysis and validated with OMI observations. *JGR Atmospheres* **125**, e2019JD030629 (2020).
16. Lafon, S., Sokolik, I. N., Rajot, J. L., Caquineau, S. & Gaudichet, A. Characterization of iron oxides in mineral dust aerosols: Implications for light absorption. *J. Geophys. Res.* **111** (2006).
17. Sokolik, I. N. & Toon, O. B. Incorporation of mineralogical composition into models of the radiative properties of mineral aerosol from UV to IR wavelengths. *J. Geophys. Res.* **104**, 9423–9444 (1999).
18. Hess, M., Koepke, P. & Schult, I. Optical properties of aerosols and clouds: the softwarE PACKAge OPAC. *Bull. Am. Meteor. Soc.* **79**, 831–844 (1998).
19. Balkanski, Y., Schulz, M., Claquin, T. & Guibert, S. Reevaluation of mineral aerosol radiative forcings suggests a better agreement with satellite and AERONET data. Atmos. Chem. Phys. **7**, 81–95 (2007). https://doi.org/10.5194/acp-7-81-2007.
20. Colarco, P. R. et al. Impact of radiatively interactive dust aerosols in the NASA GEOS-5 climate model: Sensitivity to dust particle shape and refractive index. *JGR Atmos.* **119**, 753–786 (2014).
21. Zhao, C. et al. The spatial distribution of mineral dust and its shortwave radiative forcing over North Africa: modeling sensitivities to dust emissions and aerosol size treatments. *Atmos. Chem. Phys.* **10**, 8821–8838 (2010).
22. Chen, S. et al. Modeling the transport and radiative forcing of Taklimakan dust over the Tibetan Plateau: a case study in the summer of 2006. *JGR Atmos.* **118**, 797–812 (2013).
23. Hu, Z. et al. Modeling dust sources, transport, and radiative effects at different altitudes over the Tibetan Plateau. *Atmos. Chem. Phys*. https://doi.org/10.5194/acp-20-1507-2020 (2020).
24. Adebiyi, A. A., Huang, Y., Samset, B. H. & Kok, J. F. Observations suggest that North African dust absorbs less solar radiation than models estimate. *Commun. Earth Environ.* **4**, 168 (2023).
25. Sun, H., Pan, Z. & Liu, X. Numerical simulation of spatial-temporal distribution of dust aerosol and its direct radiative effects on East Asian climate. *J. Geophys. Res.* **117**, 2011JD017219 (2012).
26. Zhang, D. F., Zakey, A. S., Gao, X. J., Giorgi, F. & Solmon, F. Simulation of dust aerosol and its regional feedbacks over East Asiausing a regional climate model. Atmos. Chem. Phys. **9**, 1095–1110 (2009). https://doi.org/10.5194/acp-9-1095-2009.
27. Mahowald, N. et al. The size distribution of desert dust aerosols and its impact on the Earth system. *Aeolian Res.* **15**, 53–71 (2014).
28. Li, L. et al. Quantifying the range of the dust direct radiative effect due to source mineralogy uncertainty. *Atmos. Chem. Phys.* **21**, 3973–4005 (2021).
29. Meng, J. et al. Improved parameterization for the size distribution of emitted dust aerosols reduces model underestimation of super coarse dust. *Geophys. Res. Lett.* **49**, e2021GL097287 (2022).
30. Song, Q. et al. Modeling impacts of dust mineralogy on fast climate response. *Atmos. Chem. Phys.* **24**, 7421–7446 (2024).
31. González-Flórez, C. et al. Insights into the size-resolved dust emission from field measurements in the Moroccan Sahara. *Atmos. Chem. Phys.* **23**, 7177–7212 (2023).
32. Kok, J. F. et al. Desert dust exerts a substantial longwave radiative forcing missing from climate models. https://doi.org/10.31223/X53B2J.
33. Zhang, X. L., Wu, G. J., Zhang, C. L., Xu, T. L. & Zhou, Q. Q. What is the real role of iron oxides in the optical properties of dust aerosols? *Atmos. Chem. Phys.* **15**, 12159–12177 (2015).
34. Miller, R. L. & Tegen, I. Radiative forcing of a tropical direct circulation by soil dust aerosols. *J. Atmos. Sci.* **56**, 2403–2433 (1999).
35. Bangalath, H. K. & Stenchikov, G. Role of dust direct radiative effect on the tropical rain belt over Middle East and North Africa: A high-resolution AGCM study. *JGR Atmos.* **120**, 4564–4584 (2015).
36. Li, L. & Sokolik, I. N. The dust direct radiative impact and its sensitivity to the land surface state and key minerals in the WRF-Chem-DuMo model: a case study of dust storms in Central Asia. *JGR Atmos.* **123**, 4564–4582 (2018).
37. Miller, R. L., Perlwitz, J. & Tegen, I. Feedback upon dust emission by dust radiative forcing through the planetary boundary layer. 56, 2403–2433.
38. Zou, X. et al. Spatial variation of topsoil features in soil wind erosion areas of northern China. *CATENA* **167**, 429–439 (2018).
39. Wu, F. et al. Saltation–sandblasting processes driving enrichment of water-soluble salts in mineral dust. *Environ. Sci. Technol. Lett.* **9**, 921–928 (2022).
40. Wu, F. et al. Surrogate atmospheric dust particles generated from dune soils in laboratory: Comparison with field measurement. *Particuology* **72**, 29–36 (2023).
41. in *Geophysical Monograph Series* (eds. Conny, J. M. & Buseck, P. R.) (Wiley, 2025) https://doi.org/10.1002/9781119554318.fmatter.

42. Castillo, M. D. et al. Field testing a low-cost passive aerosol sampler for long-term measurement of ambient PM2.5 concentrations and particle composition. *Atmos. Environ.* **216**, 116905 (2019).

43. Okada, K. & Kai, K. Atmospheric mineral particles collected at Qira in the Taklamakan Desert, China. *Atmos. Environ.* **38**, 6927–6935 (2004).

44. Hu, T. et al. Morphology and mineralogical composition of sandblasting dust particles from the Taklimakan Desert. *Sci. Total Environ.* **834**, 155315 (2022).

45. Cook, R. B., J. W., Bideaux, R. A., Bladh, K. W. & Nichols, M. C. *Handbook Mineral*. **76**, 278 (2001).

46. Formenti, P. et al. Dominance of goethite over hematite in iron oxides of mineral dust from Western Africa: Quantitative partitioning by X-ray absorption spectroscopy. *JGR Atmos.* **119** (2014).

47. Zhang H. at al. Description and Climate Simulation Performance of CAS-ESM Version 2. *J. Adv. Model Earth Syst*. **12**, e2020MS002210 (2020).

48. Wu, C. et al. Description of dust emission parameterization in CAS-ESM2 and its simulation of global dust cycle and east asian dust events. *J. Adv. Model Earth Syst.* **13**, e2020MS002456 (2021).

49. Shao, Y. Simplification of a dust emission scheme and comparison with data. *J. Geophys. Res.* **109**, 2003JD004372 (2004).

50. Mahowald, N. M. et al. Change in atmospheric mineral aerosols in response to climate: Last glacial period, preindustrial, modern, and doubled carbon dioxide climates. *J. Geophys. Res.* **111**, 2005JD006653 (2006).

51. Grini, A. & Zender, C. S. Roles of saltation, sandblasting, and wind speed variability on mineral dust aerosol size distribution during the Puerto Rican Dust Experiment (PRIDE). *J. Geophys. Res.* **109**, 2003JD004233 (2004).

52. Giles, D. M. et al. Advancements in the Aerosol Robotic Network (AERONET) Version 3 database – automated near-real-time quality control algorithm with improved cloud screening for Sun photometer aerosol optical depth (AOD) measurements. *Atmos. Meas. Tech.* **12**, 169–209 (2019).

53. Bi, J., Huang, J., Holben, B. & Zhang, G. Comparison of key absorption and optical properties between pure and transported anthropogenic dust over East and Central Asia. *Atmos. Chem. Phys.* **16**, 15501–15516 (2016).

54. Chen, S. et al. Regional modeling of dust mass balance and radiative forcing over East Asia using WRF-Chem. *Aeolian Res.* **15**, 15–30 (2014).

Acknowledgements

Author contributions

Y.-J.Y. was responsible for the composition of the main manuscript text and the preparation of the figures. C.-L.W. and H.W. were responsible for the instruction of the CAS-ESM2 simulations, while T.-F.H. and F.W. provided data classification standards. J.-J.C. contributed to the development of ideas and provided critical revisions to the manuscript. D.-Z.Z. participated in the discussion and editing. The analysis of results was conducted collectively by all authors, as was the refinement of the manuscript.

Competing interests

The authors declare no competing interests.

Additional information

Supplementary information The online version contains supplementary material available at https://doi.org/10.1038/s41612-025-01290-8.

Correspondence and requests for materials should be addressed to Junji Cao.

Reprints and permissions information is available at http://www.nature.com/reprints

Publisher's note Springer Nature remains neutral with regard to jurisdictional claims in published maps and institutional affiliations.